Visualization and manipulation of magnetic domains in the quasi-two-dimensional material Fe_3GeTe_2

Giang D. Nguyen,[1] Jinhwan Lee,[2] Tom Berlijn,[1,3] Qiang Zou,[1] Saban M. Hus,[1] Jewook Park,[1,4] Zheng Gai,[1] Changgu Lee[2,5] and An-Ping Li[1,*]

[1]*Center for Nanophase Materials Sciences, Oak Ridge National Laboratory, Oak Ridge, Tennessee 37831, USA*
[2]*School of Mechanical Engineering, Sungkyunkwan University, Suwon, Kyonggi-do 16419, Korea*
[3]*Computational Sciences & Engineering Division, Oak Ridge National Laboratory, Oak Ridge, Tennessee 37831, USA*
[4]*Center for Artificial Low Dimensional Electronic Systems, Institute for Basic Science (IBS), Pohang 37673, Korea*
[5]*SKKU Advanced Institute of Nanotechnology, Sungkyunkwan University, Suwon, Kyonggi-do 16419, Korea*

The magnetic domains in two-dimensional layered material Fe_3GeTe_2 are studied by using a variable-temperature scanning tunneling microscope with a magnetic tip after *in situ* cleaving of single crystals. A stripy domain structure is revealed in a zero-field-cooled sample below the ferromagnetic transition temperature of 205 K, which is replaced by separate double-walled domains and bubble domains when cooling the sample under a magnetic field of a ferromagnetic Ni tip. The Ni tip can further convert the double-walled domain to a bubble domain pattern as well as move the Neel-type chiral bubble in submicrometer distance. The temperature-dependent evolutions of both zero-field-cooled and field-cooled domain structures correlate well with the bulk magnetization from magnetometry measurements. Atomic resolution scanning tunneling images and spectroscopy are acquired to understand the atomic and electronic structures of the material, which are further corroborated by first-principles calculations.

I. INTRODUCTION

Magnetic two-dimensional (2D) layered materials have attracted great interest recently due to their potential application as building blocks for spintronics [1–6]. Transition metal phosphorus trisulfide (or thiophosphate), $TMPS_3$, is one of the early examples, which has been discussed as a useful candidate for the study of low-D magnetic systems [7–10]. More recently, magnetic heterostructures formed either by stacking exfoliated 2D layers or by heteroepitaxy have been actively pursued in the field of 2D materials. In these systems, the combination of spin-orbit coupling and inversion-symmetry breaking within heterostructures are expected to yield interesting spin structures and magnetoelectric transport properties [11,12]. To realize the potential of 2D magnets, a long-range magnetic order with a high transition temperature is desirable. However, layered magnetic materials often have magnetic transition temperatures below liquid nitrogen temperature. For instance, 61 and 33 K were reported for CrI_3 and $CrSiTe_3$, respectively [13,14]. In this regard, the 2D layered magnetic material Fe_3GeTe_2 is particularly interesting due to its high bulk magnetic transition temperature.

The ternary compound Fe_3GeTe_2 was reported as an itinerant ferromagnet with Curie temperatures between 220 and 230 K [15–17]. The crystal structure of Fe_3GeTe_2 is composed of Fe_3Ge heterometallic slabs that are separated by van der Waals bonded Te layers. Moreover, the Fe_3Ge slabs contain Fe(1)-Fe(1) pairs across a hexagonal network

built by Fe(2)-Ge [5,18]. The Fe(2) position was reported to have a significant concentration of vacancies (17%) [16]. The magnetic domains of Fe_3GeTe_2 were examined recently with magnetic force microscopy (MFM). Both "stripe-like bulk domains" and bubblelike domains were observed at low temperatures [17,19], and a recent report suggests an antiferromagnetic (AFM) ground state [19]. However, a clear picture of the microscopic domain structure and particularly the relationship of different types of domains remain to be investigated.

Here we study the structural and magnetic properties of Fe_3GeTe_2 using variable-temperature scanning tunneling microscope (STM) with magnetic tips [20]. STM experiments performed with magnetic tips show magnetic contrast in topographic constant-current images which resembles a domain wall contrast in MFM measurements. Both the zero-field-cooled (ZFC) and field-cooled (FC) magnetic domain structures are revealed on the surface of Fe_3GeTe_2 crystals. Besides the stripy domains found in the ZFC sample, two new types of magnetic domains are observed in the FC sample when the sample is cooled down under the stray field of the ferromagnetic Ni tip. A majority of the FC domains are double-walled domains consisting of a circular domain wall surrounded by an irregular ring-shaped domain structure, while some bubble domains appear sparsely. Interestingly, the Ni tip can be used to manipulate these magnetic domains by converting the double-walled domains into bubble domains as well as displacing the circular domain pattern inside a double-walled domain during scanning. The in-plane magnetization component of the Ni tip reveals a Neel type of 360°-domain structure. The evolution of magnetic domains as a function
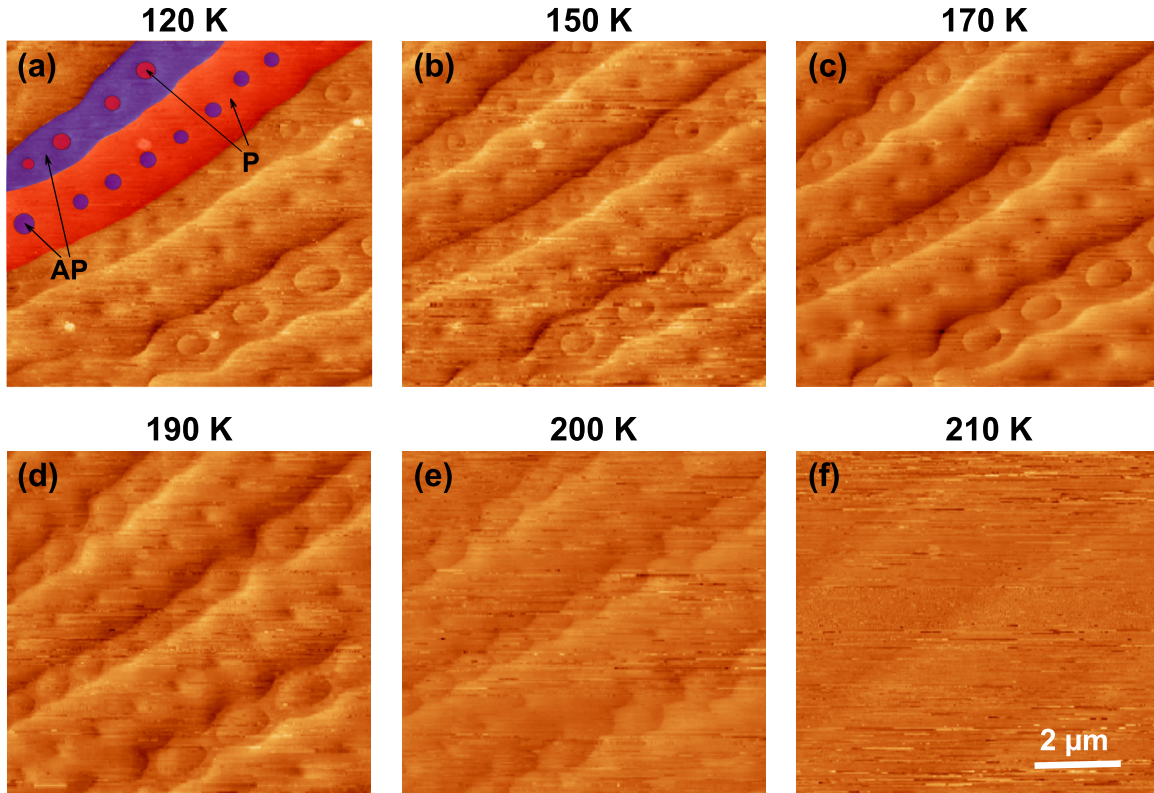
FIG. 1. The evolution of ZFC magnetic domains of cleaved Fe_3GeTe_2 visualized by STM imaging with a Ni tip while increasing sample temperature from 120 to 210 K. The semitransparent overlays in (a) illustrate the magnetizations parallel (P, red color) and antiparallel (AP, blue color) to the tip magnetization. The Ni tip is kept 10 mm away from the surface when cooling from the room temperature to 120 K to avoid the effect of Ni tip stray field on the formation of the magnetic domains. During warming up, the Ni is kept 1 μm away from the surface at the image corner. The scanning parameters are kept the same: $V_s = -0.5$ V, $I = 50$ pA.

of temperature is captured by imaging the same area during a temperature cycling. A transition temperature of 205 K is revealed for both ZFC and FC domains, consistent with magnetic measurements performed with a magnetic property measurement system (MPMS). Atomically resolved STM images and scanning tunneling spectroscopy (STS) data are compared with the first-principles calculations to provide a better understanding of the effects of Fe(2) vacancies.

II. EXPERIMENTAL DETAILS

The Fe_3GeTe_2 crystals were synthesized by the standard chemical vapor transport (CVT) method (see the Supplemental Material [21]) [15,16,19,22]. The magnetic domain images were acquired by performing topographic constant-current STM measurements with ferromagnetic Ni tips. Both non-magnetic W and ferromagnetic Ni tips were treated by a brief annealing at $\sim$400 °C before being used in STM measurement [23]. To minimize the surface contamination, single crystals of Fe_3GeTe_2 were cleaved *in situ* in ultrahigh vacuum (UHV) and then transferred directly to STM for imaging. The sample temperature in the STM is varied from 120 K to the room temperature and calibrated by using a mocking sample with a thermocouple attached. The STM tip is always kept at room temperature during all measurements [24]. All STM images were processed with WSxM software [25]. A simple parabola

flatten filter was applied to micrometer-size STM images to remove the parabolic background.

III. RESULTS

To reveal the intrinsic magnetic domain structure of the cleaved Fe_3GeTe_2 crystals, samples were cooled from room temperature to about 120 K on the STM stage. During the cooling, STM tip was fully retracted (about 10 mm away from the sample) to minimize the effects of its stray field on magnetic domains of the sample. Figure 1 shows the magnetic domains on such a ZFC sample visualized by the topographic constant-current STM with a Ni tip while varying sample temperature from 120 K to 210 K step by step. At low temperatures, stripelike domains are observed with alternative contrast corresponding to magnetization parallel (P) and antiparallel (AP) to the tip magnetization as illustrated in Fig. 1(a). These wavy stripes with rows of circular domains of opposite magnetization are typical of highly uniaxial ferromagnets whose magnetic easy axis lie along the c axis. This magnetic domain structure was observed previously on Fe_3GeTe_2 with magnetic force microscopy (MFM) [17]. As the sample temperature increases [Figs. 1(a)–1(f)], the magnetic domains remain clearly visible up to 190 K, then become dimmer at 200 K [Fig. 1(e)] and almost indistinguishable near 210 K [Fig. 1(f)]. Such an observation indicates a transition temperature T_c in the range of 200–210 K, consistent with the T_c of the Fe_3GeTe_2 reported
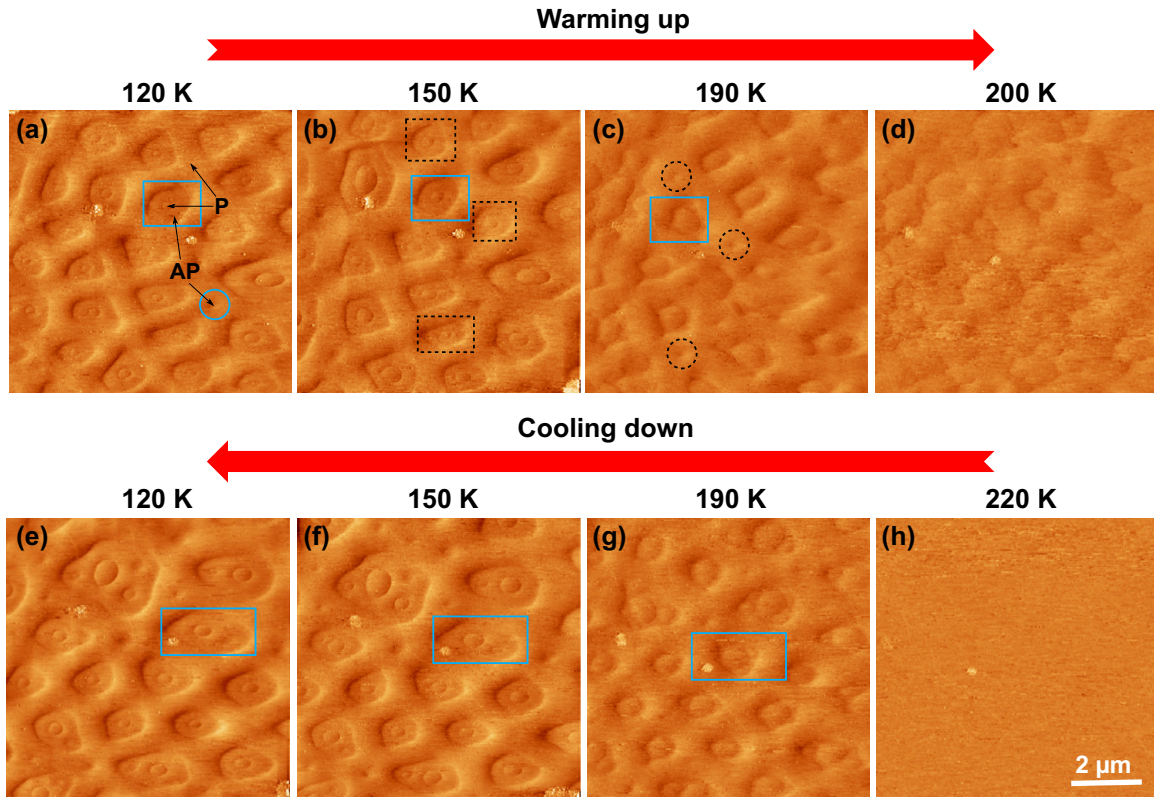
FIG. 2. The evolution of the FC magnetic domains through varying sample temperatures between 120 and 220 K. The magnetic domains were induced by keeping the Ni tip 3 μm away from the surface when cooling the sample down from the room temperature. The Ni tip is kept 1 μm away from the surface at the image corner during warming up (a–d) and cooling down (h–e). The scanning parameters are kept the same of sample bias $V_s = -0.5$ V, tunneling current $I = 50$ pA. The blue box and circle in (a) mark an example of a double-walled domain and a bubble domain, respectively. P and AP point to the domain areas with the magnetization parallel (P) and antiparallel (AP) to the tip magnetization. The dashed black circles in (c) mark the bubble domains newly converted from double-walled domains [marked by dashed black boxes in (b)] during warming from 150 to 190 K.

previously [5,15,16,19]. Also, with the increasing temperature, P domains expand their coverage at the expense of the AP domains, which becomes particularly clear at temperatures close to T_c. This behavior indicates that the stray field of Ni tip promotes the domains to align with the tip magnetization, especially at temperatures approaching the magnetic transition.

To study the effect of the stray magnetic field of the STM tip on the formation of the magnetic domains, we now examine a sample that was cooled from room temperature to 120 K with a Ni tip kept at a distance of about 3 μm above the sample surface. The measurement thus mimics a FC process. STM images taken at 120 K [Fig. 2(a)] reveal that "isolated" circular domains appear in the FC sample. This structure is quite different from the stripy magnetic domain structure observed on the ZFC sample. As discussed before for Fe$_3$GeTe$_2$ [17] and other materials [26–28], this new structure is likely to be a result of the competition between magnetostatic energy with the domain wall energy. Furthermore, these separated domains exhibit two different types of domain patterns in the STM images, specifically, double-walled domains and bubble domains. Most domains appear to have a double-walled structure where a circular domain pattern with parallel magnetization is surrounded by an irregular larger closed loop of antiparallel magnetization [see, e.g., the domain marked with a blue box in Fig. 2(a)]. In a few cases, a double-walled domain

can contain multiple circular patterns surrounded by a larger domain loop [Fig. 2(e)]. In contrast, the bubble domains [e.g., the domain marked with a blue circle in Fig. 2(a)] are randomly distributed on the surface with much lower popularity and a smaller size of about few hundred nanometers. By varying the sample temperature, we mapped changes of the magnetic domains in the same area (a complete data set can be seen in Fig. S2 in the Supplemental Material [21]). T_c of the new domain structure is found to be in the range of 200–210 K, similar to the stripy domain of ZFC samples. Furthermore, the size and shape of the double-walled domains change with temperature. As the sample temperature increases, the inner domains (with P magnetization) expand in diameter, while the outer domains (AP magnetization) shrink. This evolution of domains can be seen clearly by comparing domains marked with blue boxes in Figs. 2(a)–2(c) during warming and domains in Figs. 2(e)–2(g) during cooling, respectively. This behavior confirms that the Ni tip stray field promotes the domain alignment with the tip magnetization at higher temperature.

In addition, the double-walled domains can be converted into bubble domains during the STM scanning. Figures 3(a) and 3(b) show STM images of several domains before and after the domain conversion at 120 K, despite occurring as a low-efficiency event (less than 1%) at this temperature. At temperatures close to T_c, the probability of such a double-
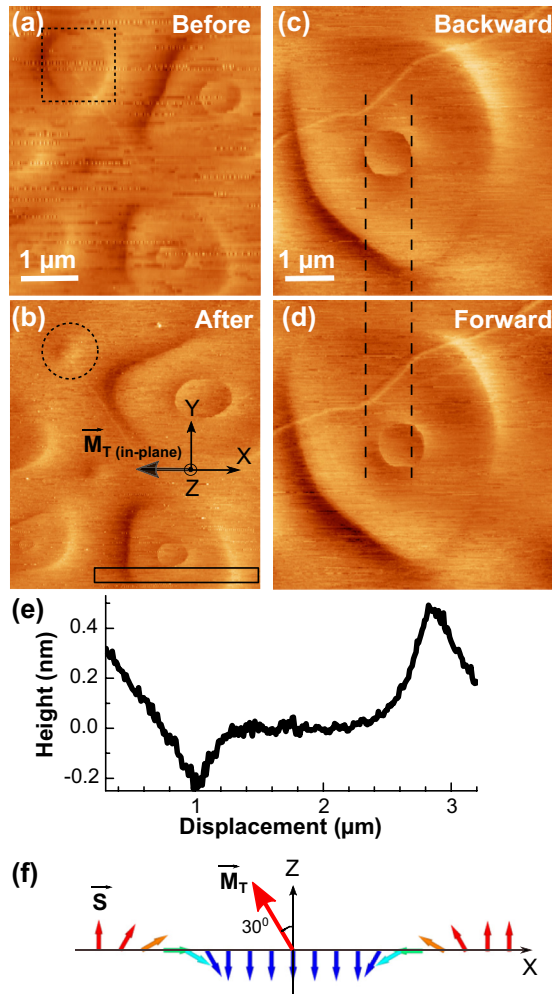
FIG. 3. (a, b) STM images of magnetic domains before (a) and after (b) tip-induced conversion of a double-walled domain (marked with dashed black box) into a bubble domain (marked with dashed black circle). (c, d) STM images of a double-walled domain showing a displacement of the inner wall between the backward (c) and the forward (d) scanned images, while the outer domain wall stays the same (sample bias $V_s = -0.5 \, \mathrm{V}$, tunneling current $I = 100 \, \mathrm{pA}$, temperature $T = 120 \, \mathrm{K}$). (e) Line profile across the outer walls of double-walled domain along the rectangle in (b). (f) Schematic spin structure of a Neel domain wall with respect to the STM tip magnetization $\vec{M}_T$.

walled to bubble domain conversion has clearly increased (to ~15%), e.g., three new bubble domains marked by dashed black circles at temperature of 190 K in Fig. 2(c) were converted from double-walled domains marked by dashed black boxes in Fig. 2(b). On the other hand, we never observed a reversed conversion from bubble domains into double-walled domains. Figures 3(c) and 3(d) show another tip manipulation effect on the inner pattern of double-walled domains at 120 K. While the outer wall stays unchanged regardless of STM scanning direction; the inner circular domain is displaced by ~150 nm between sequential forward and backward scans. The inner walls of the double-walled domain often exhibit sharp transitions across the domain wall (less than 20 nm wide), while the outer walls appear much wider (about 200 nm). A

closer look at the inner wall can be seen with a zoom-in image in Fig. S3 (see the Supplemental Material [21]) where about 10-nm noncontinuous lateral displacement of the domain wall occurs between the forward and backward scan images. The sharp transition at the inner domain walls can be attributed to the magnetic interactions of the ferromagnetic Ni tip with the domain wall that drag domain wall along with the scanning tip until it snaps off the tip and introduces a sharp transition. A similar behavior was seen in previous spin-polarized STM studies of magnetic domains on Ni(111) [29].

We note that the Ni tip we use to acquire STM images is tilted by about 30° along the -x direction (see the picture of the Ni tip in Fig. S4 in the Supplemental Material [21]). This tilted Ni tip provides STM images with large height variations about an order of magnitude higher than conventional spin-polarized STM results, and thus the spin-polarized tunneling alone cannot explain the unusually large magnetic contrast [30,31]. In fact, the height contrast enhancement was also observed in a previous STM study in layered graphite material due to the atomic force of tip-sample interaction [32]. It is possible that the surprisingly large contrast is caused by forces between the magnetic tip and the sample, which requires further investigations. The magnetic contrast is also confirmed in dI/dV spectroscopy acquired in two different magnetic domains (see Fig. S5 in the Supplemental Material [21]). The angle between magnetization axis of this tilted tip and the sample surface normal (z axis) is expected to be 30 degrees. Hence, the Ni tip has an in-plane magnetization component along $-x$ direction [Fig. 3(b)]. As shown in Figs. 3(a) and 3(b), the outer wall of the double-walled domain has a dark contrast on the left but a bright one on the right. The line profile across the outer wall of a double-walled domain is shown in Fig. 3(e) [line profiles across bubble domains also show similar character (see Fig. S7 in the Supplemental Material [21])]. Based on the azimuthal angle of the tip magnetization, we can determine whether a domain wall is of Bloch or Neel nature [33]. A dark-bright contrast at domain walls along the tip tilting direction is an indication of the 360°-Neel wall, as illustrated in Fig. 3(f), as a Bloch wall would show this dark-bright contrast in the direction orthogonal to the tip tilting direction.

Next, we compare the behavior of microscopic domains with the magnetic properties measured on the same Fe_3GeTe_2 sample by SQUID magnetometry. The magnetization hysteresis, as shown in Fig. 4(a), is anisotropic with the easy axis along the z (out-of-plane) direction. The sample has a low coercivity of 16 Oe at 80 K [Fig. 4(a) inset]. Considering the stray field of the Ni tip that can be up to 620 Oe [34], the magnetic interaction between the STM tip and the sample can indeed switch the domain magnetization and trigger the motion of domain walls. The temperature dependent magnetization measured at different conditions are shown in Fig. 4(b). In ZFC measurement, the sample was cooled down at zero field and measured under field during warming up, corresponding to our STM measurement of the intrinsic domain with Ni tip shown in Fig. 1. In both FC and field warm (FW) measurements, the sample was cooled under the field and FC curve was measured during cooling down, and FW curve was measured during warming up under external field, which corresponds to STM measurement of tip-induced domains in Fig. 2. All three curves
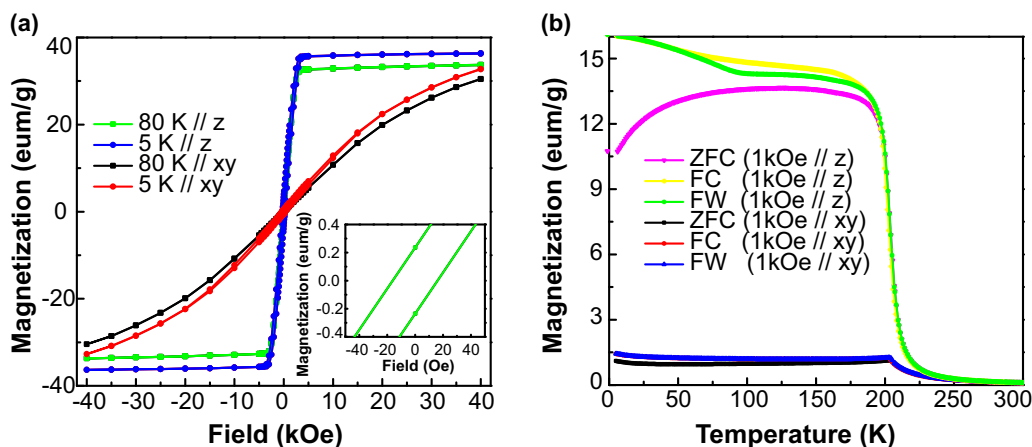
FIG. 4. (a) Field-dependent magnetization plot at 80 and 5 K. The external field is applied in $H \parallel xy$ and $H \parallel z$ directions, respectively. Inset is the zoom-in section showing coercive field for Fe_3GeTe_2 at 80 K. (b) Magnetization as a function of temperature. The applied field (1 kOe) is in $H \parallel xy$ and $H \parallel z$.

in Fig. 4(b) show the ferromagnetic transition at 205 K which is consistent with results from STM measurement.

To explore the microscopic origins of the magnetic domains, we acquired atomically resolved STM images with a nonmagnetic W tip on the cleaved Fe_3GeTe_3 surface. Figure 5(a) shows a typical image with the sixfold symmetry and a lattice constant of 0.40 ± 0.05 nm, as expected, of the top layer of Te atoms [16]. In addition, there are some randomly distributed darker regions in the STM image. The dark regions are apparently depressed by 13 to 50 pm and occupy $23 \pm 4\%$ of the surface area. These atomic domains are observed with both magnetic and non-magnetic tips and at both below and above magnetic transition temperatures (see Fig. S9 in the Supplemental Material [21]). Therefore, these atomic domains do not directly correlate with the magnetic domains observed at a larger length scale. The dI/dV spectroscopy acquired with a Ni tip show slight intensity variations across the surface, but there is no clear difference between the dark and bright atomic domains (see Fig. S10 in the Supplemental

Material [21]). The finite density states near the Fermi level confirms the metallic behavior of the material [16]. A plausible explanation for the atomic domains is the existence of atomic defects underneath the surface layer. Indeed, a previous study reported large percent of Fe(2) vacancies in the bulk crystal of Fe_3GeTe_2 [22].

To further investigate the effects of the Fe(2) vacancy, we performed Density Functional Theory (DFT) calculations with a $\sqrt{3} \times \sqrt{3}$ supercell containing a single Fe(2) vacancy (see the Supplemental Material [21] for details) [35–40]. This structure corresponds to an Fe(2) vacancy concentration of 17% which is comparable with our STM observations of about 23% as well as other experimental observations [16]. As illustrated in Fig. 5(b), we find that the nearest neighboring Te and Ge atoms displace towards the Fe(2) vacancy. In particular, the Te above the vacancy sinks 13 pm, which is roughly consistent with the height variations in the STM images. We have also performed calculations of the local density of states in a plane above the surface in the bias energy range. We found that
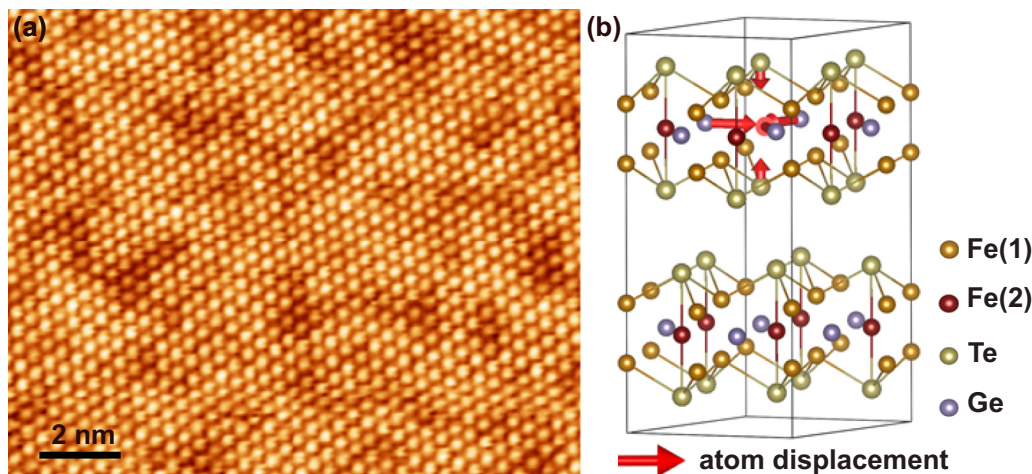

FIG. 5. (a) Atomically resolved STM image acquired with a W tip on cleaved Fe_3GeTe_2 ($V_s = -0.5$ V, $I = 100$ pA, $T = 120$ K). (b) Density functional theory results showing atomic displacements (indicated by red arrows) induced by an Fe(2) vacancy in a $\sqrt{3} \times \sqrt{3}$ supercell.
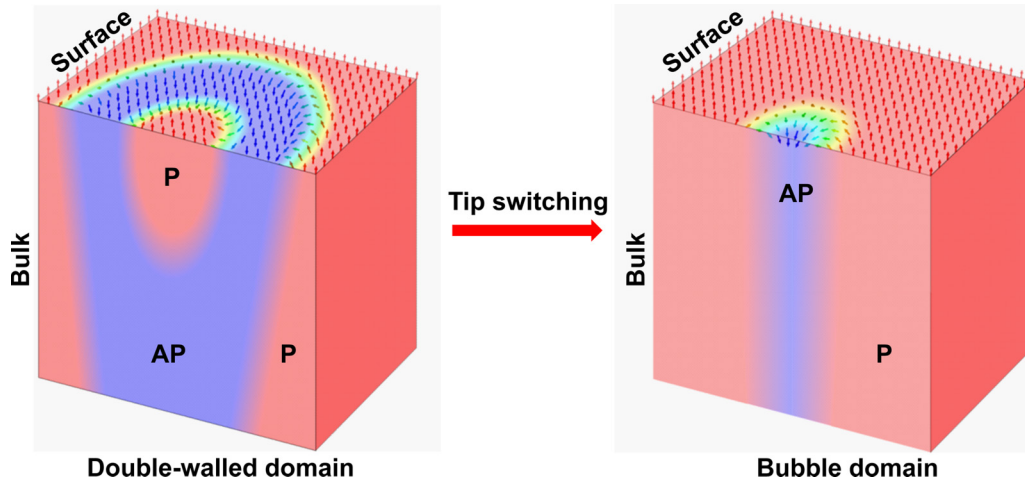
FIG. 6. The schematic micromagnetic domain structure of the FC double-walled domain and bubble domain. The blue and red colors represent two opposite magnetization directions which are antiparallel (blue) and parallel (red) to the tip magnetization, respectively.

intensities above the Fe(2) vacancies are either brighter or darker compared to those above the Fe(2) atoms depending on the absence or presence of magnetic order and the strength of onsite interaction Hubbard U corrections as implemented in the LDA + U scheme [41]. We will address these findings in a future publication. We note that the depression of the Te above the vacancy is robust against varying the magnetic state and the onsite Hubbard U interaction strength.

IV. DISCUSSION

Based on above observations, we believe that the two-phase stripy domain patterns of the ZFC sample correspond to an intrinsic behavior of Fe_3GeTe_2, as recently observed using MFM [17]. This pattern is characteristic of highly uniaxial ferromagnets at the surface perpendicular to the magnetic easy axis. In the FC sample, the stripy domain patterns morph into doubled-walled and bubble domains. Figure 6 shows schematically the proposed structures of these domains. The arrows depict the direction of spin at the spatial position, and the blue and red colors represent two opposite magnetization directions in the bulk as projected to the tip magnetization. The double-walled domain pattern contains at least three regions with two circular domain walls, while the bubble domain pattern has a bubblelike structure encompassed by a larger domain with opposite magnetization. The domain walls show 360° Neel-type character. The stray field of a magnetic tip can drive the outer domain during scanning process, which may contribute to the conversion of a double-walled domain pattern into a bubble pattern arising from the annihilation of inner domain.

We find that bubble domains in FC samples resemble magnetic chiral bubble [42] and even skyrmion structure [43]. First, the spin texture with 360° rotation across the domain (as illustrated in Fig. 6) is consistent with a Neel-type skyrmion [44–46]. Second, the emergence of the circular domain structure from stripy domain due to the stray field of the Ni tip is similar to phenomena that a magnetic field promotes the formation of skyrmion phase from a helical phase [43,47–51]. Third, the size of the bubble domain observed in this work is in the range of typical size (between 100 nm to 1 μm) of skyrmions formed due to a competition of long-range dipolar interactions with

shape anisotropy [43]. However, due to the bulk nature of the sample in this study (sample thickness in the order of 100 μm), there lacks a strong in-plane dipolar anisotropy to compete with the perpendicular easy-axis anisotropy in this material to form large sized skyrmions [42,43]. Thus, further investigation is required to confirm if the magnetic domain structures observed here have any topologically protected nature of skyrmions.

V. CONCLUSIONS

The magnetic domain structures in Fe_3GeTe_2 were investigated using STM measurements with magnetic tips, which provides a complete picture of the evolution of domains with varying sample temperatures and cooling history. In ZFC samples, a two-phase stripy magnetic domain pattern was observed at temperatures below 210 K, showing the characteristic nature of highly uniaxial ferromagnets with a surface perpendicular to the magnetic easy axis. In addition to these intrinsic domains, new magnetic domain structures with a double-walled domain and a bubble domain patterns were discovered in FC samples. The magnetic domains can be manipulated using a ferromagnetic STM tip to convert the double-walled domain into a bubble domain. This tip-induced domain conversion and manipulation opens the possibility of writing magnetic domains on this quasi-2D layered material, a capability that would be of great value in information technology [52]. The domain walls show 360° Neel wall character which resembles skyrmion-like chiral structure. The atomically resolved STM images in combination with DFT calculations confirmed the existence of Fe vacancies, which provides insight into the understanding of the magnetic transitions in this technologically interesting quasi-2D material.

[1] G. R. Bhimanapati *et al.*, ACS Nano **9**, 11509 (2015).
[2] M. Enayat *et al.*, Science **345**, 653 (2014).
[3] C. Gong *et al.*, Nature **546**, 265 (2017).
[4] S. M. Hus and A.-P. Li, Prog. Surf. Sci. **92**, 176 (2017).
[5] A. F. May, S. Calder, C. Cantoni, H. Cao, and M. A. McGuire, Phys. Rev. B **93**, 014411 (2016).
[6] K. Novoselov, A. Mishchenko, A. Carvalho, and A. C. Neto, Science **353**, aac9439 (2016).
[7] R. Clement, J. J. Girerd, and I. Morgenstern-Badarau, Inorg. Chem. **19**, 2852 (1980).
[8] P. A. Joy and S. Vasudevan, Phys. Rev. B **46**, 5425 (1992).
[9] A. R. Wildes *et al.*, Phys. Rev. B **92**, 224408 (2015).
[10] K.-Z. Du, X.-Z. Wang, Y. Liu, P. Hu, M. I. B. Utama, C. K. Gan, Q. Xiong, and C. Kloc, ACS Nano **10**, 1738 (2016).
[11] A. G. Swartz, P. M. Odenthal, Y. Hao, R. S. Ruoff, and R. K. Kawakami, ACS Nano **6**, 10063 (2012).
[12] H. X. Yang, A. Hallal, D. Terrade, X. Waintal, S. Roche, and M. Chshiev, Phys. Rev. Lett. **110**, 046603 (2013).
[13] M. A. McGuire, H. Dixit, V. R. Cooper, and B. C. Sales, Chem. Mater. **27**, 612 (2015).
[14] V. Carteaux, F. Moussa, and M. Spiesser, Europhys. Lett. **29**, 251 (1995).
[15] B. Chen, J. Yang, H. Wang, M. Imai, H. Ohta, C. Michioka, K. Yoshimura, and M. Fang, J. Phys. Soc. Jpn. **82**, 124711 (2013).
[16] H.-J. Deiseroth, K. Aleksandrov, C. Reiner, L. Kienle, and R. K. Kremer, Eur. J. Inorg. Chem. **2006**, 1561 (2006).
[17] N. León-Brito, E. D. Bauer, F. Ronning, J. D. Thompson, and R. Movshovich, J. Appl. Phys. **120**, 083903 (2016).
[18] J.-X. Zhu *et al.*, Phys. Rev. B **93**, 144404 (2016).
[19] J. Yi *et al.*, 2D Mater. **4**, 011005 (2017).
[20] R. Wiesendanger, Rev. Mod. Phys. **81**, 1495 (2009).
[21] See Supplemental Material at http://link.aps.org/supplemental/10.1103/PhysRevB.97.014425 for detailed descriptions of material synthesis and theoretical calculations and additional STM and STS data.
[22] V. Y. Verchenko, A. A. Tsirlin, A. V. Sobolev, I. A. Presniakov, and A. V. Shevelkov, Inorg. Chem. **54**, 8598 (2015).
[23] J. Park, C. Park, M. Yoon, and A.-P. Li, Nano Lett. **17**, 292 (2017).
[24] J. Park, G. He, R. M. Feenstra, and A.-P. Li, Nano Lett. **13**, 3269 (2013).
[25] I. Horcas, R. Fernández, J. Gomez-Rodriguez, J. Colchero, J. Gómez-Herrero, and A. Baro, Rev. Sci. Instrum. **78**, 013705 (2007).

[26] B. Roberts and C. Bean, Phys. Rev. **96**, 1494 (1954).
[27] J. B. Goodenough, Phys. Rev. **102**, 356 (1956).
[28] J. Jeong *et al.*, Phys. Rev. B **92**, 054426 (2015).
[29] L. Dzemiantsova *et al.*, Phys. Rev. B **84**, 205431 (2011).
[30] R. Wiesendanger, H. J. Güntherodt, G. Güntherodt, R. J. Gambino, and R. Ruf, Phys. Rev. Lett. **65**, 247 (1990).
[31] R. Wiesendanger, I. V. Shvets, D. Bürgler, G. Tarrach, H. J. Güntherodt, J. M. D. Coey, and S. Gräser, Science **255**, 583 (1992).
[32] J. M. Soler, A. M. Baro, N. García, and H. Rohrer, Phys. Rev. Lett. **57**, 444 (1986).
[33] A. Kubetzka, O. Pietzsch, M. Bode, and R. Wiesendanger, Phys. Rev. B **67**, 020401 (2003).
[34] M. Rastei and J. Bucher, J. Phys.: Condens. Matter **18**, L619 (2006).
[35] K. Momma and F. Izumi, J. Appl. Crystallogr. **44**, 1272 (2011).
[36] G. Kresse and D. Joubert, Phys. Rev. B **59**, 1758 (1999).
[37] J. P. Perdew, K. Burke, and M. Ernzerhof, Phys. Rev. Lett. **77**, 3865 (1996).
[38] G. Kresse and J. Furthmüller, Phys. Rev. B **54**, 11169 (1996).
[39] P. E. Blöchl, Phys. Rev. B **50**, 17953 (1994).
[40] H. J. Monkhorst and J. D. Pack, Phys. Rev. B **13**, 5188 (1976).
[41] S. L. Dudarev, G. A. Botton, S. Y. Savrasov, C. J. Humphreys, and A. P. Sutton, Phys. Rev. B **57**, 1505 (1998).
[42] A. Fernández-Pacheco, R. Streubel, O. Fruchart, R. Hertel, P. Fischer, and R. P. Cowburn, Nat. Commun. **8**, 15756 (2017).
[43] N. Nagaosa and Y. Tokura, Nat. Nanotechnol. **8**, 899 (2013).
[44] I. Kézsmárki *et al.*, Nat. Mater. **14**, 1116 (2015).
[45] N. Romming, A. Kubetzka, C. Hanneken, K. von Bergmann, and R. Wiesendanger, Phys. Rev. Lett. **114**, 177203 (2015).
[46] K. von Bergmann, K. André, P. Oswald, and W. Roland, J. Phys.: Condens. Matter **26**, 394002 (2014).
[47] X. Yu, Y. Onose, N. Kanazawa, J. Park, J. Han, J. Matsui, N. Nagaosa, and Y. Tokura, Nature **465**, 901 (2010).
[48] X. Yu, N. Kanazawa, Y. Onose, K. Kimoto, W. Zhang, S. Ishiwata, Y. Matsui, and Y. Tokura, Nat. Mater. **10**, 106 (2011).
[49] X. Yu, M. Mostovoy, Y. Tokunaga, W. Zhang, K. Kimoto, Y. Matsui, Y. Kaneko, N. Nagaosa, and Y. Tokura, Proc. Natl. Acad. Sci. U.S.A. **109**, 8856 (2012).
[50] G. Yu *et al.*, Nano Lett. **16**, 1981 (2016).
[51] C. Felser, Angew. Chem., Int. Ed. **52**, 1631 (2013).
[52] E. Meyer, H. J. Hug, and R. Bennewitz, *Scanning Probe Microscopy: The Lab on a Tip* (Springer Science & Business Media, Berlin, 2013).